Exploring the Origin of Anionic Redox Activity in the Super Li-rich Iron Oxide Based High-Energy-Density Cathode Materials

Zhenpeng Yao,[1234*] Maria K. Y. Chan,[5] Chris Wolverton[2*]

[1]*Center of Hydrogen Science, Shanghai Jiao Tong University, 800 Dongchuan Road, Shanghai 200240, China*

[2]*Department of Material Science and Engineering, Northwestern University, 2220 Campus Drive, Evanston, Illinois 60208, United States*

[3]*The State Key Laboratory of Metal Matrix Composites, School of Materials Science and Engineering, Shanghai Jiao Tong University, 800 Dongchuan Road, Shanghai 200240, China*

[4]*Innovation Center for Future Materials, Zhangjiang Institute for Advanced Study, Shanghai Jiao Tong University, 429 Zhangheng Road, Shanghai 201203, China*

[5]*Center for Nanoscale Materials, Argonne National Laboratory, Argonne, Illinois 60439, United States*

* *Correspondence: c-wolverton@northwestern.edu, z.yao@sjtu.edu.cn*

Abstract

Super alkali-rich materials (alkali: transition metal ≥ 2:1), such as Li_5FeO_4, exhibit the potential to realize anionic redox upon deep delithiation. Recently, Li_5FeO_4 was shown to undergo reversible cycling between $Li_4FeO_{3.5}$ and $Li_3FeO_{3.5}$ with a combined cation/anion redox, a remarkable capacity of 189 mAh/g, and no O_2 release. However, the energetic impact of the phase transformations on the reaction thermodynamics as well as the correlation between the structural changes and reaction reversibility remain unclear. In this study, we use first-principles calculations to examine the delithiation and (re-)lithiation reactions of the Li_5FeO_4. We show that the experimentally observed charge and discharge processes go through non-equilibrium pathways. Upon delithiation, the compound undergoes a phase transformation from Li_5FeO_4, with tetrahedrally coordinated (T_d) Fe-ions, to a delithiated disordered rocksalt structure, with octahedral (O_h) Fe ions. Fe ion migration has an asymmetric kinetic barrier which makes $T_d \rightarrow O_h$ migration facile, whereas the reverse process has a much larger barrier, explaining the difficulties in reaction reversibility. We further elucidate the transition metal and O redox sequences during the charge cycle and identify the complex electrochemistry associated with the dual participation of cationic redox (Fe^{3+}/Fe^{4+}) and anionic redox ($O^{2-}/O^{1-}/O^0$). Armed with this knowledge, we conduct high-throughput screening of all the known alkali rich transition metal oxides by evaluating their potential to enable reversible anionic redox, with multiple candidates proposed for further experimental trials. Our work provides a useful guide on the further development of super-alkali-rich anionic-redox-active electrodes for high-energy-density batteries.

1. Introduction

The pursuit of electric vehicles (EVs) with extended range that can compete with conventional internal combustion engine automobiles coupled with efforts to incorporate renewable energy technologies into the national electric grid demands electrochemical energy storage devices with higher energy density, lower cost, and longer cycle life.[1–3] Cathodes of state-of-the-art rechargeable batteries including lithium-ion batteries (LIBs) and sodium-ion batteries (SIBs), are typically lithium/sodium transition metal (TM) oxides[4] such as $LiNi_{1-x-y}Mn_xCo_yO_2$ (NMC)[5] and $Na_{2/3}Ni_{1/3}Mn_{2/3}O_2$,[6] which store (release) electrical energy *via* alkali ion extraction and re-accommodation, accompanied by redox reactions of TM cations. The specific capacity of the electrode is therefore limited by the number of electrons per TM cation that can participate in the redox reaction. To boost the capacity and energy density, anionic redox reactivity with oxygen ions complementarily providing the charge-compensating electrons was introduced to the rechargeable battery chemistry. Enhanced capacities achieved through anionic redox have been reported for various systems including Li_4FeSbO_6,[7] Li_3NbO_4,[8] Li_3IrO_4,[9] $Li_4Mn_2O_5$,[10] $Li_4(Mn,M)_2O_5$ (M = transition metals),[11] Li_5FeO_4,[12] β-Li_2IrO_3,[13] $Li_2Mn_{1-y}M_yO_2F$,[14] $Na_{2/3}Mg_{0.28}Mn_{0.72}O_2$,[15] $Na_{4/7-x}[\square_{1/7}Mn_{6/7}]O_2$ (□ = vacancy),[16] $NaLi_{1/3}Mn_{2/3}O_2$,[17] and disordered high-entropy rocksalt ($Li_{1.3}Mn_{0.4}Ti_{0.1}Nb_{0.2}O_{1.7}F_{0.3}$ and $Li_{1.3}Mn_{0.2}Co_{0.1}Cr_{0.1}Ti_{0.1}Nb_{0.2}O_{1.7}F_{0.3}$).[18] Significant efforts have since been made to understand the origin of the oxygen redox with insight obtained on the structural and chemical features of anion-redox-active systems such as the formation of peroxo-like $(O_2)^{n-}$ species,[19,20] local alkali-excess environments, [11,12,21,22] and O hole numbers per oxygen[23]. The local alkali-excess environments are particularly attractive as they can be intentionally incorporated through cationic disordering of the electrode structure.[22] The

exploration of new anionic-active chemistries to increase capacity, reduce cost, and eliminate O_2 release is continuing and has received significant attention from the battery community.

Super alkali-rich materials such as Li_2IrO_3,[13] Li_3NbO_4,[8] Li_5FeO_4,[24] Li_6CoO_4,[24] Li_8ZrO_6,[25] and $Na_2Ru_{1-y}Sn_yO_3$,[26] Na_5FeO_4,[27] which feature an extra high alkali content (A = alkali elements, A:TM ≥ 2:1), show great potential to enable the anionic redox activity during electrochemical cycling. Complete charge of super alkali-rich materials, if possible, would require more charge-compensating electrons (greater than $2e^-$ per TM) than those provided by the limited redox capabilities of the TM ions (generally no more than $2e^-$ per TM), necessitating the participation of oxygen redox. However, initial attempts of many super alkali-rich materials as cathodes resulted in poor capacity with minimal alkali (de-)intercalated reversibly (such as Li_5FeO_4 and Li_6CoO_4).[24] In addition, complex phase transformations can occur during (de-)lithiation, and O_2 release and reaction metastability are often involved.[25] Progress was achieved by Trahey *et al.* with a Li_5FeO_4-based Li-ion/Li–O_2 hybrid cathode, in which 4 Li and 2 O (O_2 releasing) were extracted and re-accommodated during charge and discharge in a Li/Li_5FeO_4–O_2 cell (**Eq. 1**); however, the hybrid chemistry resulted in poor cyclability.[28–30]

$$Li_5FeO_4 \rightarrow 4Li^+ + 4e^- + O_2 + LiFeO_2 \quad (1)$$

$$\text{i. } Li_5FeO_4 \rightarrow 2Li + 2e^- + 0.25O_2 + Li_3FeO_{3.5} \quad (2)$$

$$\text{ii. } Li_3FeO_{3.5} \rightarrow 1Li + 1e^- + 0.25O_2 + Li_2FeO_3 \quad (3)$$

$$\text{iii. } Li_2FeO_3 \rightarrow 1Li + 1e^- + 0.5O_2 + LiFeO_2 \quad (4)$$

The delithiation mechanism of Li_5FeO_4 was examined in detail through a series of experimental studies.[12,31,32] The first charge process of Li_5FeO_4 was observed to proceed through a three-step phase transformation: Li_5FeO_4 (antifluorite) → disordered rocksalt $Li_3FeO_{3.5}$ (DR1) → disordered rocksalt Li_2FeO_3 (DR2) → amorphous $LiFeO_2$, as expressed by **Eq. 2–4**. Recently,

Zhan *et al.* discovered that the re-lithiation of $Li_3FeO_{3.5}$ is feasible with 1 Li accommodated and reversible cycling between $Li_4FeO_{3.5}$ and $Li_3FeO_{3.5}$ is achieved with a decent capacity of 189 mAh/g and no O_2 release (**Eq. 5**),[12] which is higher than the $LiCoO_2$ electrode (~140 mAh/g)[33] and comparable to the renown NMC electrode ($LiNi_{0.8}Mn_{0.1}Co_{0.1}$, ~200mAh/g).[5]

$$\text{iv. } Li_4FeO_{3.5} \leftrightarrow 1Li + 1e^- + Li_3FeO_{3.5} \quad (5)$$

Despite this breakthrough, the energetic impact of the phase transformation on the reaction thermodynamics as well as any correlation between the structural changes and reaction irreversibility remain unclear, thereby warranting further investigation. Moreover, to understand the origin of the improved electrochemical cyclability with the well-controlled oxygen evolution, a thorough investigation of the Fe/O redox mechanisms and local oxygen environments during the reaction is necessary, which will shed light on the potential activation and application of other super alkali-rich materials.

First-principles density functional theory (DFT) calculations have accelerated the discovery of battery materials by enabling the determination of thermodynamic evolution and mass transport during electrochemical reactions,[34–37] revealing the underlying mechanisms in the specific electrochemistry,[38,39] and predicting new high-performance electrode materials.[40–42] In this study, we first simulate the delithiation and (re-)lithiation of Li_5FeO_4 by constructing the Li–Fe–O phase diagram. The experimentally observed delithiation and (re-)lithiation are predicted to proceed *via* non-equilibrium pathways, with the calculated corresponding voltage profile showing remarkable agreement with the experimentally obtained charging curve. We then investigate the origin of the "off-equilibrium" reaction pathways and the delithiation irreversibility by examining the TM (Fe) migration energetics. The Fe migration required for the phase transition from the antifluorite to disordered rocksalt structure is associated with an anisotropic kinetic barrier, with a

small forward barrier and a much larger backward barrier, leading to difficulty for the reverse phase transition, thereby impairing the reaction reversibility and causing the delithiation reactions to proceed in a non-equilibrium manner. We further elucidate the TM and O redox sequences during the charge cycle and identify the complex electrochemistry involving the participation of cationic redox (Fe^{3+}/Fe^{4+}) and anionic redox ($O^{2-}/O^{1-}/O^{0}$), validating the experimental observations. We were able to confirm the Li-coordinated only O configuration as the active redox center and these active sites can be introduced intentionally by the phase transition from a distinct (antifluorite) one to the disordered rocksalt phase. Finally, based on this mechanism, we conduct a high-throughput study on all known alkali transition metal oxides and explore their potential to enable the anionic redox activity with multiple candidates identified for further trials. We are able to identify Li_2PbO_3, Li_2SnO_3, Li_3IrO_4, Li_3NbO_4, Li_2MoO_3, Li_2MnO_3, Li_2RhO_3, Na_2PtO_3, Na_3RuO_4, Li_2RuO_3 as candidates for the potential synthesis of disordered rocksalt phase and Li_5FeO_4, Li_4PbO_4, Li_2MoO_4, Li_4TiO_4, Li_3VO_4, Li_2CrO_4, Li_6CoO_4, $Na_7Fe_3O_8$, Na_2FeO_4, Na_4TiO_4, Na_2CrO_4, Na_2MoO_4, Na_2MnO_2 to experience potential electrochemical activation upon initial charge, to ultimately unlock the anionic redox activity. Our discoveries are expected to provide guidance and testable predictions for experimental studies of simultaneous cation/anion redox in high-energy-density electrodes.

2. Methodology

2.1 First-principles calculations

All the first-principles DFT calculations reported in this study were conducted using the Vienna Ab-initio Simulation Package (VASP)[43–46] with projector augmented wave (PAW) potentials[47] and the Perdew–Burke–Ernzerhof (PBE)[48] exchange-correlation functional. A plane-wave basis with a cutoff energy of 520 eV and ***Γ***-centered *k*-meshes with a density of 8000 *k*-points

per reciprocal atom were used for all the calculations. All the calculations were spin-polarized, with Fe atoms initialized in a high-spin ferromagnetic configuration and relaxed to self-consistency. The DFT + *U* method introduced by Dudarev *et al.*[49] was used to treat the localized 3*d* electrons of Fe with a *U* value of 4.0, obtained by fitting to experimental and calculated formation enthalpies in a previous study.[50] To simulate the migration of Fe ions, climbing image nudged elastic band (CI-NEB)[51,52] calculations were performed to determine the diffusion pathway geometry and transition-state energetic information. The high-throughput screening was conducted under the framework of the Open Quantum Materials Database (OQMD).[53]

2.2 Voltage profile calculations

The average charge/discharge voltage (relative to A/A^+) can be computed using the negative of the reaction free energy per A added/removed, as shown in **Eq. 6**:[54,55]

$$V = \frac{\Delta G_{\mathrm{f}}}{F\Delta N_{\mathrm{A}}}, \tag{6}$$

where F is the Faraday constant, ΔN_{A} is the amount of Li/Na added/removed, and ΔG_{f} is the (molar) change in free energy of the reaction. Considering a two-phase reaction between A_xMO_y and $A_{x'}MO_{y'}$, $A_xMO_y + (x' - x)\ A \rightarrow A_{x'}MO_{y'}$, ΔG_{f} can be approximated by the total internal energy ΔE from DFT calculations,

$$\Delta E = E\left(A_xMO_y\right) - E\left(A_{x'}MO_{y'}\right) - (x - x')E(A_{\mathrm{metal}}) - (y - y')E(O_{\mathrm{gas}}), \tag{7}$$

where $E\left(A_xMO_y\right)$ and $E\left(A_{x'}MO_{y'}\right)$ are the DFT energies at the respective compositions.

3. Results and discussion

3.1 Phase evolution and reaction thermodynamics during charge/discharge of Li_5FeO_4

Electrochemical charge/discharge of super alkali-rich materials can be chemically and structurally complicated with the possible existence of non-equilibrium phases.[25] Phase diagrams

represent the thermodynamic phase equilibria of multicomponent systems and provide useful information on the electrochemical reactions between phases. To obtain a thorough understanding of the reaction thermodynamics during the delithiation of Li_5FeO_4, we constructed the Li–Fe–O T = 0 K phase diagram using structures with the lowest energy for each composition. All compounds in the Inorganic Crystal Structure Database (ICSD) in the Li–Fe–O chemical space were used.[56] The elemental reference states (Li, Fe, non-solid O_2) were obtained by fitting[57] to experimental formation energies, mainly from two major databases, the SGTE substance database (SSUB) and a database constructed by Nash *et al*.[58–60] Experimentally observed disordered rocksalt phases, $Li_4FeO_{3.5}$, $Li_3FeO_{3.5}$, Li_2FeO_3, and amorphous $LiFeO_2$, were also included, with the corresponding computational unit cells built using the special quasi-random structure (SQS) method.[61] Starting from the cubic rock-salt cell, supercells containing 30 cation/30 anion sites, 56 cation/56 anion sites, and 27 cation/27 anion sites were created for $Li_4FeO_{3.5}$, $Li_3FeO_{3.5}$, and Li_2FeO_3, respectively. We randomly populated the cation sites with Fe and Li in ratios of 4:1, 3:1, and 2:1 for $Li_4FeO_{3.5}$, $Li_3FeO_{3.5}$, and Li_2FeO_3, respectively. Vacancies were randomly introduced to the anion sites of the $Li_4FeO_{3.5}$ and $Li_3FeO_{3.5}$ structures in ratios of 3:7 and 1:7 with respect to O, and all the anion sites of Li_2FeO_3 were occupied by O. All the SQSs were generated using a Monte Carlo algorithm implemented in the ATAT package[62–64] with the constraint that the pair and triplet correlation functions of the SQS were identical to those of the statistically random Li/Fe population of cation sites and O/vacancy population of anion sites at least up to the third nearest neighbor. To create a supercell of amorphous $LiFeO_2$ suitable for DFT calculations, a cell containing 96 atoms was melted at 2900 K in an *ab initio* molecular dynamics simulation. The liquid-state configuration was equilibrated over 2 ps under an NVT ensemble,[34] followed by rapid quenching from the equilibration temperature to 300 K at a rate of 1 K fs^{-1}. Then, the atomic coordinates and cell

parameters of the configuration were relaxed in the DFT calculation until the average forces fell below 10^{-2} eV $Å^{-1}$.[35]

The Li–Fe–O phase diagram (T = 0 K) is presented in **Fig. 1a** with the ground-state stable compounds (*i.e.*, the compounds with energy lower than any other linear combination of structures) marked by black circles. One intermediate phase is identified as stable on the convex hull between Li_5FeO_4 and $LiFeO_2$ (**Fig. 1b**): Li_2FeO_3(C2/m) with the following equilibrium Li_5FeO_4 delithiation reaction pathway (purple, Fig. 1a): Li_5FeO_4(Pbca) → Li_2FeO_3(C2/m) → $LiFeO_2$ ($I4_1/amd$). However, all the experimentally observed delithiated phases, $Li_3FeO_{3.5}$(DR1), Li_2FeO_3(DR2), and $LiFeO_2$ (amorphous) (**Fig. 1a**, shown as red crosses), are predicted to have energies higher than the mixture of the stable phases by 75, 129, and 144 meV/atom, respectively (**Fig. 1b**). The experimentally observed delithiation pathway, Li_5FeO_4 (Pbca) → $Li_3FeO_{3.5}$ (DR1) → Li_2FeO_3 (DR2) → $LiFeO_2$ (amorphous), is therefore thermodynamically unstable or "non-equilibrium" (red, **Fig. 1ab**), unlike the equilibrium pathway. The calculated voltage profile corresponding to the non-equilibrium reaction pathway shows significantly improved agreement with the experimentally obtained charging curve compared with its equilibrium delithiation counterpart (**Fig. 1c**). In addition, the re-lithiated phase $Li_4FeO_{3.5}$ (DR3) is also predicted to be unstable (133 meV/atom above the convex hull), suggesting that the reversible (re-)lithiation reactions between $Li_3FeO_{3.5}$ (DR1) and $Li_4FeO_{3.5}$ (DR3) are also non-equilibrium (**Fig. 1ab**, blue). Understanding the origin of the "off-equilibrium" reaction pathways is thus essential. In the following section, we will explore the energetic impacts of the structural changes during the phase transformation on both the reaction thermodynamics and reversibility.

3.2 Structural change, reaction irreversibility, and initial O release

At the beginning of the delithiation reaction of Li_5FeO_4, a phase transition from antifluorite Li_5FeO_4 to disordered rocksalt $Li_3FeO_{3.5}$ (DR1) occurs, as expressed in **Eq. 2**a, which is known to be irreversible. We studied the phase transition by examining the structural changes during the first step of delithiation. In the antifluorite Li_5FeO_4, O ions form an *fcc* array, and Fe and Li ions occupy 6 of the 8 tetrahedral (T_d) interstitial sites (**Fig. 2a**). In addition, in the disordered rocksalt $Li_3FeO_{3.5}$ (DR1), O ions (vacancies) still form an *fcc* array, and Fe and Li ions occupy all the octahedral (O_h) interstitial sites (**Fig. 2a**). As a result, Fe ions and remaining Li ions during the first reaction step must migrate from the O_h sites to the T_d sites with an associated activation energy, which is expected to become more energetically favorable with decreasing Li content because the phase transition takes place as charging occurs. We then start with the original antifluorite Li_5FeO_4 unit cell (8 f.u.) and move one Fe ion to its nearby O_h vacancy while removing its surrounding Li ions. We monitor the energy difference E_{diff} between two $Li_{5-x}FeO_4$ antifluorite structures: (i) a structure in which one Fe ion is moved to the O_h sites and (ii) a structure in which all the Fe ions remain in the T_d sites. Unexpectedly, although E_{diff} shows some decreasing trend (**Fig. 2b**), it remains positive regardless of the number of removed surrounding Li ions (x = 0–5), indicating that it is energetically unfavorable for Fe to sit in the O_h sites, contrary to our speculation. Considering that Fe is not only neighbored by Li but also O ions, O ion contributions should also be taken into account.

As illustrated in **Fig. 2a**, the Fe migration path is surrounded by a number of different O ions. We examined the effect of O on the Fe migration by calculating another energy difference E_{diff}' between two $Li_5FeO_{4-\delta}$ antifluorite structures: (i) a structure in which one Fe ion is moved to the O_h sites and (ii) a structure in which all the Fe ions remain in T_d sites, both with one surrounding O ion removed. A small E_{diff}' suggests the strong hindrance of the specific O ion to the Fe

migration, making the migration more viable after removing it. We calculated the E_{diff}' values corresponding to the removal of each O ion while recording the Fe–O distance changes upon Fe migration. The results (**Tab. 1**) indicate that it is actually the O ***a*** ion, located directly on the extended tie line between the Fe O_h and T_d site, that causes the strongest Fe migration blockage. In addition, the O ***a*** ion experiences the largest Fe–O distance change upon Fe migration, and the Fe–O bond must thus be completely broken before the migration. We then take out the O ***a*** ion and recalculate all the E_{diff} values, which become negative after two Li ions are removed, consistent with the experimentally observed phase transition point $x = 2$, indicating that the extraction of O enables the Fe migration and initiates the phase transformation.

To find the saddle point and minimum energy path during the Fe migration at the phase transition point ($x = 2$), we calculated the kinetic barrier using the NEB method.[51,52] Fe migration from the T_d site to the nearby O_h site was observed to be highly anisotropic (**Fig. 2c**): the forward barrier that enables the phase transformation from the antifluorite to disordered rocksalt structure is small (0.25 eV), whereas the backward barrier is large (0.90 eV), explaining the difficulty of the inverse phase transformation from the disordered rocksalt back to the antifluorite structure as well as the observed poor reversibility of **Eq. 2** during discharge. With the Fe migration anisotropy in mind, we can now understand the origin of the "off-equilibrium" delithiation pathway of Li_5FeO_4. With Li and O removal upon delithiation, Fe will spontaneously migrate to enable the reaction from Li_5FeO_4 (Pbca) → $Li_3FeO_{3.5}$ (DR1). In the equilibrium Li_2FeO_3 (C2/m) structure, O ions (vacancies) also form an *fcc* array while Fe and Li ions occupy all the octahedral (O_h) interstitial sites in an ordered manner. Possible further delithiation of $Li_3FeO_{3.5}$ (DR1) to the equilibrium Li_2FeO_3 (C2/m) structure therefore requires a large amount of Fe migration from one O_h site to another to realize ordering among Fe ions. A large portion of the migrating Fe ions may encounter

the large backward diffusion barrier and become blocked. Then, the cationic disordering of the system will remain with the delithiation between two disordered phases $Li_3FeO_{3.5}$ (DR1) → Li_2FeO_3 (DR2) occurring *via* solid-solution reactions. With increasingly more Li and O vacancies introduced into the system, it will ultimately lose stability and becomes amorphous ($x = 4$, $LiFeO_2$). With the understanding that the TM (Fe) migration is strongly correlated to the electrochemical reaction reversibility and non-equilibrium reaction pathways, a similar situation should be avoided when searching for other super Li-rich candidates for LIB electrodes.

3.3 Competing TM/O redox couple, local structure, and origin of anionic activity

The reversible re-lithiation of $Li_3FeO_{3.5}$ (DR1) to $Li_4FeO_{3.5}$ (DR3) produces a new type of Fe-oxide-based anionic-redox-active electrode material. Understanding the origin of the reversible O redox activity is thus essential for both improvement of the Li_5FeO_4-based electrode and the search for novel anionic redox active materials. We monitored the evolution of the oxidation states of Fe and O ions during delithiation (**Eq. 2–4**) and re-lithiation (**Eq. 5**) by comparing the calculated magnetizations of Fe and O ions with the number of unpaired electrons of the corresponding ions with known oxidation states. The numbers of unpaired electrons for Fe^{3+} (tetrahedrally coordinated), Fe^{4+} (octahedrally coordinated), and Fe^{5+} (octahedrally coordinated) are 5, 4, and 3, respectively, as shown in **Fig. 3a**. In the original Li_5FeO_4 phase, the magnetizations are approximately 4.1 for all the Fe ions, implying an overall 3+ oxidation state. After 2 Li ions and a small amount of O were extracted ($x = 2$, $y = 0.5$), 7/14 (total) Fe ions showed magnetizations of approximately 3.5 (**Fig. 3a**), indicating that half of the Fe ions had been oxidized to 4+. The Fe magnetization distribution remained almost constant after the extraction of 3 Li and 1 O per formula unit ($x = 3$, $y = 1$). In the final phase ($x = 4$, $y = 2$), most of the Fe ions (22 of 25) exhibited magnetizations of approximately 4.1, corresponding to an oxidation state of 3+ and indicating the

reduction of most Fe^{4+} by additional O removal. Three Fe ions showed smaller magnetizations of approximately 3.5 and 3, corresponding to oxidation states of 4+ and 5+, which is expected considering the complex local environments for specific Fe ions in the amorphous structure. During the re-lithiation of $Li_3FeO_{3.5}$ to $Li_4FeO_{3.5}$ (x = 1, y = 0.5), all the Fe ions exhibited magnetizations of approximately 4.0, confirming the complete reduction of Fe^{4+} to Fe^{3+}, as observed experimentally.[12] For the oxygen ions, the magnetizations in the original Li_5FeO_4 are close to 0, corresponding to an overall valence state of 2− for oxygen ions. After the extraction of 2 Li and 0.5 O per formula unit (x = 2, y = 0.5), several oxygen ions (7 of 49) exhibited increased magnetizations of approximately 0.5 (**Fig. 3b**), indicating the partial oxidation of O^{2-} to O^{1-}. With further Li and O removal (x = 3, y = 1), a similar portion of oxygen ions (4 of 27) showed increased magnetizations. In the final phase (x = 4, y = 2), a relatively wide distribution of the magnetizations of oxygen ions was observed, corresponding to the various oxygen-ion local environments in the amorphous structure. No oxygen ions exhibited magnetization above ~0.4, indicating an overall oxidation state of 2− for the oxygen ions. In the critical re-lithiated phase ($Li_4FeO_{3.5}$), all the oxygen ions exhibited magnetizations of approximately 0 again, indicating the full reduction of O^{1-} to O^{2-}. We thus have a detailed understanding of the competing Fe/O redox during the delithiation and confirmed the simultaneous cationic and anionic redox, as observed in a previous experimental study.[12] About the detailed re-lithiation process of the DR $Li_3FeO_{3.5}$ phase, many mechanisms have been put forward.[65,66] Yet further experimentally observations, especially the accurate position refinement of Li and O ions upon re-lithiation, are still demanded.

To identify the origin of the O redox activity, we then examined the local atomic environments and electronic states of active O ions in all the delithiated and re-lithiated phases: $Li_3FeO_{3.5}$ (DR1), Li_2FeO_3 (DR2), and $Li_4FeO_{3.5}$ (DR3). All the O^{1-} ions were identified as being

in the particular "A_6–O" configuration (**Fig. 3c**) with only Li-ion coordination (first nearest neighbors), with the remaining oxygen ions remaining as O^{2-} with at least one Fe first nearest neighbor (**Fig. 3e**). The projected DOS (*p*DOS) of the oxygen 2*p* states and Fe 3*d* states of these two configurations are shown in **Figs. 3c-e**. For the A_6–O configuration (**Fig. 3c**), the contribution from oxygen to the valence band immediately below the Fermi level is significantly larger than that from Fe, indicating that electrons can be readily extracted from oxygen when the system is oxidized. In contrast, for the partially Fe-coordinated configurations (**Fig. 3e**), the Fe–O bonds show strong covalency, and both cationic and anionic activities can be expected during further charging. In addition, the cationic/ionic redox occurring during delithiation can be qualitatively determined from the locations of the holes generated by extracting electrons. The isosurface shown in the inset of **Fig. 3c** was constructed by visualizing the charge density in the energy range between 0 and −1 eV, which roughly corresponds to the removal of one electron. Apparently, the hole is localized around the oxygen atom in the center of A_6–O, which signals the ionic redox behavior. This result indicates that on further delithiation, the O^{1-} in the local Li-excess environment originating from this particular A_6–O configuration can give out one labile electron (**Fig. 3d**) and become O^0, consistent with a previous study.[22] The irreversible delithiation from $Li_3FeO_{3.5}$ (DR1) to Li_2FeO_3 (DR2) and $LiFeO_2$ (amorphous) proceeds *via* the gradual oxidation of O^{1-} to O^0 and the elimination of these specific A_6–O configurations (**Fig. 3f**). Nevertheless, these A_6–O configurations would be retained during the re-lithiation to $Li_4FeO_{3.5}$ (DR3), with the oxygen ions being reduced to O^{2-}. As shown in **Fig. 3d**, the Fe contribution to the states lying below the Fermi level is almost negligible compared with that from oxygen, and the isosurface corresponding to the removal of one electron is also centered around the oxygen ion; therefore, significant anionic redox can be expected. The extraction of labile electrons from the A_6–O

configuration enables the reversible partial oxidation of O^{2-} to O^{1-}. The O^{2-}/O^{1-} redox couple in this specific configuration, along with the Fe^{3+}/Fe^{4+} redox couple, thus play a key role during the reversible cycling between $Li_4FeO_{3.5}$ and $Li_3FeO_{3.5}$. In the original antifluorite Li_5FeO_4 structure, O ions exclusively located in the non-A_6–O configurations (**Fig. 3f**) and all the A_6–O configurations are generated during the first phase transition and the introduction of cationic disordering to the system. Thus, the first phase transition step can be seen as the "activation" process of the Li_5FeO_4 electrode system. Particular attention should be paid to searching for the possible existence of an activation process in the use of other types of super alkali-rich materials as electrode materials.

3.4 High-throughput screening for super A-rich oxide based anionic-redox electrodes

As described in the previous section, the local alkali excess A_6–O configuration serves as the redox center to enable the reversible anionic redox activity upon the cycling of the super A-rich iron oxide. To search for more super A-rich anionic-redox electrodes aiming at improved performance through the same mechanism, we conduct high-throughput screening on all experimentally reported ternary super A-rich oxides (containing single transition metal) from the ICSD database[56] by estimating their possibility of being introduced with the A_6–O configurations. The ternary super Li-rich materials family currently consists of more than 60 compounds with new members announced continuously and our screening results should also shed light on the design of multinary systems.[56] There are known multi-transition metal compounds existing, like the famous $Li_2Ru_ySn_{1-y}O_3$;[67] unfortunately, their structures are either not refined completely or not publicly shared. The alkali excess configuration is not observed in any ordered alkali transition metal oxide structures, including the A-rich oxides. Even at the highest A:TM ratio of eight (*e.g.*, Li_8IrO_6), every oxygen atom bonds directly to the transition metal atom. The introduction of the

A_6–O "Li/Na-coordinated only" configurations necessitates the formation of disordered rocksalt structured super A-rich oxides *via* activation (like here for $Li_4FeO_{3.5}$[12]) or direct synthesis.

Synthesizing cation-disordered versions of alkali transition metal oxides has been suggested to be effective upon the unlocking of anionic redox such as disordered $Li_{(1+x)}Ti_{2x}Fe_{(1-3x)}O_2$,[68] disordered $Li_{1.25}Nb_{0.25}Mn_{0.5}O_2$,[69] cation-disordered Li_3NbO_4,[70] and so on. Considering that the disordered rocksalt versions of transition metal oxides are usually higher in energy than their ordered equilibrium counterparts,[11] corresponding synthesis demands more energetic methods like ball milling.[8,10] Recently, an ultrafast sintering method was developed, which shows promise to synthesize even far-from-equilibrium phases with synthesis temperature as high as 3273K and a fast temperature variation speed.[71] Meanwhile, the synthesizability of disordered rocksalt (DR) structured super A-rich oxides can be estimated by computing the free energy difference relative to their ordered ground state phases: $\Delta G = G_{DR} - G_{ordered} = \Delta E - T\Delta S^{conf}$ while a ΔG less than zero indicates the energetic favorability of the disordered phase. We calculate the energy difference: $\Delta E = E_{DR} - E_{ordered}$, where E_{DR} is the total energy of simulated DR structure obtained with the special quasi-random structure (SQS) method[61] and $E_{ordered}$ is the total energy of the ordered ground state phase. Configurational entropy is computed as follows: $\Delta S^{conf} = \Delta S_{DR}{}^{conf} - \Delta S_{ordered}{}^{conf} = k_B(x_A\mathbf{ln}(x_A) + x_{TM}\mathbf{ln}(x_{TM}))$. As an evaluation of the synthesizability upper limit of the disordered rocksalt phases, we set the temperature to be the new high synthesis temperature record of 3273 K.[71] Free energy differences then have been determined for all super A-rich oxides which have both A and TM located at the octahedral positions while O forms the *fcc* backbone (**Fig. 4a**). We would prefer the compounds where the disordered phase can drop down below the ground state for temperatures of 3273K. We assumed that synthesis of the DR version of oxides with A or TM preferring positions beyond octahedral would be even less feasible with extra energy required on

potential bond breaking and mass transport. We are able to identify Li_2PbO_3, Li_2SnO_3, Li_3IrO_4, Li_3NbO_4, Li_2MoO_3, Li_2MnO_3, Li_2RhO_3, Na_2PtO_3, Li_2RuO_3 as the candidates for potential DR phase synthesis, which exhibit the promise for unlocking the anionic redox activity. Among them, cation disordered rocksalt (DR) Li_3NbO_4[70] and Li_3IrO_4[9] have been reported with anionic redox activity and large capacity, validating our hypothesis. Li_2MnO_3,[72] Li_2RhO_3,[73] Li_2RuO_3,[74] Li_2SnO_3[74] are well-known anionic redox layered electrodes while their DR comparts haven't been tried yet and thus are worth exploring. Li_2MoO_3[75] also adopts a layered structure and was found to experience Mo migration from the metal layer to the lithium layer during slow and irreversible delithiation. Then there is a trend for it to transfer into a DR compound, which may even make its cycling reversible. Furthermore, Li_2PbO_3 and Na_2PtO_3 haven't ever been tried for lithium delithiation study and demand further study.

The other approach to bring alkali excess configurations to the oxides is electrochemical activation, as we observed during the initial Li and O removal of Li_5FeO_4. The geometrically and energetically asymmetric iron migration triggering the phase transition of the A-rich iron oxide from antifluorite to disordered rocksalt, creating these anionic redox active A_6-O centers. Therefore, we hypothesize that A-rich oxides, which show notable trends to have asymmetric transition metal ion migrations (from tetrahedral to octahedral) upon charge, are inclined to experience a phase transition to the disordered rocksalt. Prediction of the migration trend using methods like the crystal field theory during a combined A/O removal is challenging because of the unclear valence variations of the metal ions (*e.g.*, $Fe^{3+} \longrightarrow Fe^{3+}/Fe^{4+} \longrightarrow Fe^{3+}$ for $Li_5FeO_4 \longrightarrow LiFeO_2$). Here we estimate the transition metal migration trend of oxides by examining their closest neighbors' metal positions in the A-TM-O phase diagram with both A and O removed. For example, in the Li-Fe-O phase diagram, Li_5FeO_4 (space group: Pbca) with Fe located in the

tetrahedral position has a closest neighbor of Li_2FeO_3 (space group: C2/m) with Fe located in the octahedral position (**Fig. 4b**). Although actual delithiation doesn't follow the equilibrium pathway, the equilibrium product still gives essential information on the local coordinates. We then construct phase diagrams for all super A-rich oxides and search for their nearest neighbors with results shown in **Tab. 2**. Calculations to construct equilibrium Li-M-O phase diagrams were carried out within the Open Quantum Materials Database (OQMD) framework.[53] We prefer compounds having TM at T_d sites which also are connected on the convex hull to a phase with TM at the O_h sites. Among all known super A-rich oxides, we are able to identify Li_5FeO_4, Li_4PbO_4, Li_2MoO_4, Li_4TiO_4, Li_3VO_4, Li_2CrO_4, Li_6CoO_4, $Na_7Fe_3O_8$, Na_2FeO_4, Na_4TiO_4, Na_2CrO_4, Na_2MoO_4, Na_2MnO_2, which are candidates to experience an electrochemical activation upon charge and unlocking their anionic redox activity (**Fig. 4c**). Li_5FeO_4 is the compound which we build this hypothesis from. Similar to Li_5FeO_4, Li_6CoO_4 also experiences an irreversible lithium removal during its first charge along with a phase transition to an unidentified intermediate phase, which then deserves a thorough investigation as we did for Li_5FeO_4.[24] Li_4PbO_4, Li_2MoO_4, Li_4TiO_4, Li_3VO_4, Li_2CrO_4, $Na_7Fe_3O_8$, Na_2FeO_4, Na_4TiO_4, Na_2CrO_4, Na_2MoO_4, Na_2MnO_2 haven't been tested for their delithiation behavior and thus demands further experimental exploration.

Additionally, a natural next step of this work would be exploring the potential existence of substituted super Li-rich compounds, such as $Li_2M_yM'_{1-y}O_3$ through DFT, validating their synthesizability, and measuring their performance *via* experiments, respectively. However, we believe that is out of the scope of this study.

4. Conclusions

In this study, we explored the structural and electrochemical properties of Li_5FeO_4-based super alkali-rich cathode materials using first-principles DFT calculations. We simulated the

charge and discharge of Li_5FeO_4 by building the Li–Fe–O phase diagram. The experimentally observed charge and discharge were predicted to proceed *via* non-equilibrium pathways. The origin of the "off-equilibrium" reaction pathways and the reaction irreversibility were then investigated by examining the TM (Fe) migration energetics. The Fe migration required by the phase transition from the antifluorite to disordered cubic structure, is associated with an anisotropic kinetic barrier, leading to difficulty for the reverse phase transition, thereby impairing the reaction reversibility and causing the delithiation reactions to proceed in a non-equilibrium manner. We further elucidated the TM and O redox sequences during the charge cycle and identified a complex electrochemistry with the participation of competing cationic redox (Fe^{3+}/Fe^{4+}) and anionic redox ($O^{2-}/O^{1-}/O^{0}$). Finally, we conducted high-throughput screening on all known alkali-rich transition metal oxides and provide suggestions for further development of super-A-rich anionic-redox-active electrode materials for rechargeable batteries. We are able to identify Li_2PbO_3, Li_2SnO_3, Li_3IrO_4, Li_3NbO_4, Li_2MoO_3, Li_2MnO_3, Li_2RhO_3, Na_3RuO_4, Na_2PtO_3, Li_2RuO_3 as the candidates for potential DR phase synthesis and Li_5FeO_4, Li_4PbO_4, Li_2MoO_4, Li_4TiO_4, Li_3VO_4, Li_2CrO_4, Li_6CoO_4, $Na_7Fe_3O_8$, Na_2FeO_4, Na_4TiO_4, Na_2CrO_4, Na_2MoO_4, Na_2MnO_2 to experience potential electrochemical activation upon initial charge, to ultimately unlock the anionic redox activity. Our theoretical findings provide valuable insights on the structural and electrochemical behavior of alkali-rich Li_5FeO_4 cathode materials and will be beneficial in the design of next-generation high-energy-density cathode materials.

References

(1) Thackeray, M. M.; Wolverton, C.; Isaacs, E. D. Electrical Energy Storage for Transportation-Approaching the Limits of, and Going Beyond, Lithium-Ion Batteries.

Energy Environ. Sci. **2012**, *5* (7), 7854–7863.

(2) Van der Ven, A.; Deng, Z.; Banerjee, S.; Ong, S. P. Rechargeable Alkali-Ion Battery Materials: Theory and Computation. *Chem. Rev.* **2020**, *120* (14), 6977–7019.

(3) Xiao, Y.; Wang, Y.; Bo, S.-H.; Kim, J. C.; Miara, L. J.; Ceder, G. Understanding Interface Stability in Solid-State Batteries. *Nat. Rev. Mater.* **2020**, *5* (2), 105–126.

(4) Zhao, C.; Wang, Q.; Yao, Z.; Wang, J.; Sánchez-Lengeling, B.; Ding, F.; Qi, X.; Lu, Y.; Bai, X.; Li, B.; et al. Rational Design of Layered Oxide Materials for Sodium-Ion Batteries. *Science (80-.).* **2020**, *370* (6517), 708–711.

(5) Ohzuku, T.; Makimura, Y. Layered Lithium Insertion Material of LiCo1/3Ni1/3Mn1/3O2 for Lithium-Ion Batteries. *Chem. Lett.* **2001**, *30* (7), 642–643.

(6) Paulsen, J. M.; Donaberger, R. A.; Dahn, J. R. Layered T2-, O6-, O2-, and P2-Type A(2/3)[M'2+(1/3)M4+(2/3)]O2 Bronzes, A = Li, Na; M' = Ni, Mg; M = Mn, Ti. *Chem. Mater.* **2000**, *12* (8), 2257–2267.

(7) McCalla, E.; Sougrati, M. T.; Rousse, G.; Berg, E. J.; Abakumov, A.; Recham, N.; Ramesha, K.; Sathiya, M.; Dominko, R.; Van Tendeloo, G.; et al. Understanding the Roles of Anionic Redox and Oxygen Release during Electrochemical Cycling of Lithium-Rich Layered Li4FeSbO6. *J. Am. Chem. Soc.* **2015**, *137* (14), 4804–4814.

(8) Yabuuchi, N.; Takeuchi, M.; Nakayama, M.; Shiiba, H.; Ogawa, M.; Nakayama, K.; Ohta, T.; Endo, D.; Ozaki, T.; Inamasu, T.; et al. High-Capacity Electrode Materials for Rechargeable Lithium Batteries: Li3NbO4-Based System with Cation-Disordered Rocksalt Structure. *Proc. Natl. Acad. Sci. U. S. A.* **2015**, *112* (25), 7650–7655.

(9) Perez, A. J.; Jacquet, Q.; Batuk, D.; Iadecola, A.; Saubanère, M.; Rousse, G.; Larcher, D.; Vezin, H.; Doublet, M.-L.; Tarascon, J.-M. Approaching the Limits of Cationic and

Anionic Electrochemical Activity with the Li-Rich Layered Rocksalt Li3IrO4. *Nat. Energy* **2017**, *2* (12), 954–962.

(10) Freire, M.; Kosova, N. V.; Jordy, C.; Chateigner, D.; Lebedev, O. I.; Maignan, A.; Pralong, V. A New Active Li–Mn–O Compound for High Energy Density Li-Ion Batteries. *Nat. Mater.* **2016**, *15* (2), 173–177.

(11) Yao, Z.; Kim, S.; He, J.; Hegde, V. I.; Wolverton, C. Interplay of Cation and Anion Redox in Li4Mn2O5 Cathode Material and Prediction of Improved Li4(Mn,M)2O5 Electrodes for Li-Ion Batteries. *Sci. Adv.* **2018**, *4* (5), eaao6754.

(12) Zhan, C.; Yao, Z.; Lu, J.; Ma, L.; Maroni, V. A.; Li, L.; Lee, E.; Alp, E. E.; Wu, T.; Wen, J.; et al. Enabling the High Capacity of Lithium-Rich Anti-Fluorite Lithium Iron Oxide by Simultaneous Anionic and Cationic Redox. *Nat. Energy* **2017**, *2* (12), 963–971.

(13) Pearce, P. E.; Perez, A. J.; Rousse, G.; Saubanère, M.; Batuk, D.; Foix, D.; McCalla, E.; Abakumov, A. M.; Van Tendeloo, G.; Doublet, M.-L.; et al. Evidence for Anionic Redox Activity in a Tridimensional-Ordered Li-Rich Positive Electrode β-Li2IrO3. *Nat. Mater.* **2017**, *16* (5), 580–586.

(14) Lee, J.; Kitchaev, D. A.; Kwon, D.-H.; Lee, C.-W.; Papp, J. K.; Liu, Y.-S.; Lun, Z.; Clément, R. J.; Shi, T.; McCloskey, B. D.; et al. Reversible Mn2+/Mn4+ Double Redox in Lithium-Excess Cathode Materials. *Nature* **2018**, *556* (7700), 185–190.

(15) Yabuuchi, N.; Hara, R.; Kubota, K.; Paulsen, J.; Kumakura, S.; Komaba, S. A New Electrode Material for Rechargeable Sodium Batteries: P2-Type Na2/3[Mg0.28Mn0.72]O2 with Anomalously High Reversible Capacity. *J. Mater. Chem. A* **2014**, *2* (40), 16851–16855.

(16) Mortemard de Boisse, B.; Nishimura, S.; Watanabe, E.; Lander, L.; Tsuchimoto, A.;

Kikkawa, J.; Kobayashi, E.; Asakura, D.; Okubo, M.; Yamada, A. Highly Reversible Oxygen-Redox Chemistry at 4.1 V in Na4/7−x[□ 1/7Mn6/7O2 (□: Mn Vacancy). *Adv. Energy Mater.* **2018**, *8* (20), 1800409.

(17) Wang, Q.; Mariyappan, S.; Rousse, G.; Morozov, A. V; Porcheron, B.; Dedryvère, R.; Wu, J.; Yang, W.; Zhang, L.; Chakir, M.; et al. Unlocking Anionic Redox Activity in O3-Type Sodium 3d Layered Oxides via Li Substitution. *Nat. Mater.* **2021**, *20* (3), 353–361.

(18) Lun, Z.; Ouyang, B.; Kwon, D.-H.; Ha, Y.; Foley, E. E.; Huang, T.-Y.; Cai, Z.; Kim, H.; Balasubramanian, M.; Sun, Y.; et al. Cation-Disordered Rocksalt-Type High-Entropy Cathodes for Li-Ion Batteries. *Nat. Mater.* **2021**, *20* (2), 214–221.

(19) McCalla, E.; Abakumov, A. M.; Saubanère, M.; Foix, D.; Berg, E. J.; Rousse, G.; Doublet, M.-L.; Gonbeau, D.; Novák, P.; Van Tendeloo, G.; et al. Visualization of O-O Peroxo-like Dimers in High-Capacity Layered Oxides for Li-Ion Batteries. *Science (80-.).* **2015**, *350* (6267), 1516–1521.

(20) Grimaud, A.; Hong, W. T.; Shao-Horn, Y.; Tarascon, J.-M. Anionic Redox Processes for Electrochemical Devices. *Nat. Mater.* **2016**, *15* (2), 121–126.

(21) Luo, K.; Roberts, M. R.; Hao, R.; Guerrini, N.; Pickup, D. M.; Liu, Y.-S.; Edström, K.; Guo, J.; Chadwick, A. V.; Duda, L. C.; et al. Charge-Compensation in 3d-Transition-Metal-Oxide Intercalation Cathodes through the Generation of Localized Electron Holes on Oxygen. *Nat. Chem.* **2016**, *8* (7), 684–691.

(22) Seo, D.-H.; Lee, J.; Urban, A.; Malik, R.; Kang, S.; Ceder, G. The Structural and Chemical Origin of the Oxygen Redox Activity in Layered and Cation-Disordered Li-Excess Cathode Materials. *Nat. Chem.* **2016**, *8* (7), 692–697.

(23) Ben Yahia, M.; Vergnet, J.; Saubanère, M.; Doublet, M. L. Unified Picture of Anionic

Redox in Li/Na-Ion Batteries. *Nat. Mater.* **2019**, *18* (5), 496–502.

(24) Narukawa, S. Anti-Fluorite Type Li6CoO4, Li5FeO4, and Li6MnO4 As the Cathode for Lithium Secondary Batteries. *Solid State Ionics* **1999**, *122* (1–4), 59–64.

(25) Huang, S.; Wilson, B. E.; Wang, B.; Fang, Y.; Buffington, K.; Stein, A.; Truhlar, D. G. Y-Doped Li8ZrO6: A Li-Ion Battery Cathode Material with High Capacity. *J. Am. Chem. Soc.* **2015**, *137* (34), 10992–11003.

(26) Rozier, P.; Sathiya, M.; Paulraj, A. R.; Foix, D.; Desaunay, T.; Taberna, P. L.; Simon, P.; Tarascon, J. M. Anionic Redox Chemistry in Na-Rich Na2Ru1 - YSnyO3 Positive Electrode Material for Na-Ion Batteries. *Electrochem. commun.* **2015**, *53*, 29–32.

(27) Hoppe, R.; Brachtel, G. Neue Oxoferrate(III). Zur Kenntnis von Na5FeO4. *Zeitschrift fuer Anorg. und Allg. Chemie* **1978**, *446*, 10.

(28) Trahey, L.; Johnson, C. S.; Vaughey, J. T.; Kang, S.-H.; Hardwick, L. J.; Freunberger, S. A.; Bruce, P. G.; Thackeray, M. M. Activated Lithium-Metal-Oxides as Catalytic Electrodes for Li–O2 Cells. *Electrochem. Solid-State Lett.* **2011**, *14* (5), A64.

(29) Johnson, C. S.; Kang, S.-H.; Vaughey, J. T.; Pol, S. V.; Balasubramanian, M.; Thackeray, M. M. Li2O Removal from Li5FeO4: A Cathode Precursor for Lithium-Ion Batteries. *Chem. Mater.* **2010**, *22* (3), 1263–1270.

(30) Thackeray, M. M.; Chan, M. K. Y.; Trahey, L.; Kirklin, S.; Wolverton, C. Vision for Designing High-Energy, Hybrid Li Ion/Li-O2 Cells. *J. Phys. Chem. Lett.* **2013**, *4* (21), 3607–3611.

(31) Okumura, T.; Shikano, M.; Kobayashi, H. Effect of Bulk and Surface Structural Changes in Li 5 FeO 4 Positive Electrodes during First Charging on Subsequent Lithium-Ion Battery Performance. *J. Mater. Chem. A* **2014**, *2* (30), 11847.

(32) Harada, K.; Hibino, M.; Kobayashi, H.; Ogasawara, Y.; Okuoka, S.; Yonehara, K.; Ono, H.; Sumida, Y.; Yamaguchi, K.; Kudo, T.; et al. Electrochemical Reactions and Cathode Properties of Fe-Doped Li2O for the Hermetically Sealed Lithium Peroxide Battery. *J. Power Sources* **2016**, *322*, 49–56.

(33) Mizushima, K.; Jones, P. C.; Wiseman, P. J.; Goodenough, J. B. LixCoO2 (0<x<1):A New Cathode Material for Batteries of High Energy Density. *Mater. Res. Bull.* **1980**, *15* (6), 783–789.

(34) Kang, K.; Meng, Y. S.; Bréger, J.; Grey, C. P.; Ceder, G.; Ceder, G. Electrodes with High Power and High Capacity for Rechargeable Lithium Batteries. *Science (80-.).* **2006**, *311* (5763), 977–980.

(35) Li, Q.; Liu, H.; Yao, Z.; Cheng, J.; Li, T.; Li, Y.; Wolverton, C.; Wu, J.; Dravid, V. P. Electrochemistry of Selenium with Sodium and Lithium: Kinetics and Reaction Mechanism. *ACS Nano* **2016**, *10* (9), 8788–8795.

(36) Urban, A.; Seo, D.-H.; Ceder, G. Computational Understanding of Li-Ion Batteries. *npj Comput. Mater.* **2016**, *2* (1), 16002–16014.

(37) Morgan, D.; Van der Ven, A.; Ceder, G. Li Conductivity in LixMPO4 (M = Mn, Fe, Co, Ni) Olivine Materials. *Electrochem. Solid-State Lett.* **2004**, *7* (2), A30–A32.

(38) Li, Q.; Xu, Y.; Yao, Z.; Kang, J.; Liu, X.; Wolverton, C.; Hersam, M. C.; Wu, J.; Dravid, V. P. Revealing the Effects of Electrode Crystallographic Orientation on Battery Electrochemistry via the Anisotropic Lithiation and Sodiation of ReS2. *ACS Nano* **2018**, *12* (8), 7875–7882.

(39) Hwang, S.; Yao, Z.; Zhang, L.; Fu, M.; He, K.; Mai, L.; Wolverton, C.; Su, D. Multistep Lithiation of Tin Sulfide: An Investigation Using in Situ Electron Microscopy. *ACS Nano*

2018, *12* (4), 3638–3645.

(40) Yu, H.-C.; Ling, C.; Bhattacharya, J.; Thomas, J. C.; Thornton, K.; Van der Ven, A. Designing the next Generation High Capacity Battery Electrodes. *Energy Environ. Sci.* **2014**, *7* (5), 1760–1768.

(41) Jain, A.; Hautier, G.; Moore, C. J.; Ping Ong, S.; Fischer, C. C.; Mueller, T.; Persson, K. A.; Ceder, G. A High-Throughput Infrastructure for Density Functional Theory Calculations. *Comput. Mater. Sci.* **2011**, *50* (8), 2295–2310.

(42) Curtarolo, S.; Hart, G. L. W.; Nardelli, M. B.; Mingo, N.; Sanvito, S.; Levy, O. The High-Throughput Highway to Computational Materials Design. *Nat. Mater.* **2013**, *12* (3), 191–201.

(43) Kresse, G.; Hafner, J. Ab Initio Molecular Dynamics for Liquid Metals. *Phys. Rev. B* **1993**, *47*, 558–561.

(44) Kresse, G.; Hafner, J. Ab Initio Molecular-Dynamics Simulation of the Liquid-Metal-Amorphous-Semiconductor Transition in Germanium. *Phys. Rev. B* **1994**, *49* (20), 14251–14269.

(45) Kresse, G.; Furthmüller, J. Efficiency of Ab-Initio Total Energy Calculations for Metals and Semiconductors Using a Plane-Wave Basis Set. *Comput. Mater. Sci.* **1996**, *6*, 15–50.

(46) Kresse, G. Efficient Iterative Schemes for Ab Initio Total-Energy Calculations Using a Plane-Wave Basis Set. *Phys. Rev. B* **1996**, *54* (16), 11169–11186.

(47) Blöchl, P. E. Projector Augmented-Wave Method. *Phys. Rev. B* **1994**, *50* (24), 17953–17979.

(48) Perdew, J. P.; Ernzerhof, M.; Burke, K. Rationale for Mixing Exact Exchange with Density Functional Approximations. *J. Chem. Phys.* **1996**, *105* (22), 9982–9985.

(49) Dudarev, S. L.; Savrasov, S. Y.; Humphreys, C. J.; Sutton, A. P. Electron-Energy-Loss Spectra and The Structural Stability of Nickel Oxide: An LSDA+U Study. *Phys. Rev. B* **1998**, *57* (3), 1505–1509.

(50) Wang, L.; Maxisch, T.; Ceder, G. Oxidation Energies of Transition Metal Oxides within the GGA+U Framework. *Phys. Rev. B* **2006**, *73* (19), 195107–195112.

(51) Michel, K. J.; Ozoliņš, V. Vacancy Diffusion in NaAlH4 and Na3AlH6. *J. Phys. Chem. C* **2011**, *115* (43), 21465–21472.

(52) Michel, K. J.; Wolverton, C. Symmetry Building Monte Carlo-Based Crystal Structure Prediction. *Comput. Phys. Commun.* **2014**, *185* (5), 1389–1393.

(53) Kirklin, S.; Saal, J. E.; Meredig, B.; Thompson, A.; Doak, J. W.; Aykol, M.; Rühl, S.; Wolverton, C. The Open Quantum Materials Database (OQMD): Assessing the Accuracy of DFT Formation Energies. *npj Comput. Mater.* **2015**, *1*, 15010–15024.

(54) Aydinol, M. K.; Kohan, A. F.; Ceder, G.; Cho, K.; Joannopoulos, J. Ab Initio Study of Lithium Intercalation in Metal Oxides and Metal Dichalcogenides. *Phys. Rev. B* **1997**, *56* (3), 1354–1365.

(55) Wolverton, C.; Zunger, A. First-Principles Prediction of Vacancy Order-Disorder and Intercalation Battery Voltages in LixCoO2. *Phys. Rev. Lett.* **1998**, *81* (3), 606–609.

(56) Belsky, A.; Hellenbrandt, M.; Karen, V. L.; Luksch, P. New Developments in the Inorganic Crystal Structure Database (ICSD): Accessibility in Support of Materials Research and Design. *Acta Crystallogr. Sect. B Struct. Sci.* **2002**, *58* (3), 364–369.

(57) Grindy, S.; Meredig, B.; Kirklin, S.; Saal, J. E.; Wolverton, C. Approaching Chemical Accuracy with Density Functional Calculations: Diatomic Energy Corrections. *Phys. Rev. B* **2013**, *87* (7), 075150–075157.

(58) Stevanović, V.; Lany, S.; Zhang, X.; Zunger, A. Correcting Density Functional Theory for Accurate Predictions of Compound Enthalpies of Formation: Fitted Elemental-Phase Reference Energies. *Phys. Rev. B* **2012**, *85* (11), 115104–115115.

(59) SGTE. *Thermodynamic Properties of Inorganic Materials*; Berlin, Heidelberg, 1999.

(60) Nash, P. Thermodynamic Database. *https://tptc.iit.edu/index.php/thermo-database* **2013**.

(61) Zunger, A.; Wei, S.; Ferreira, L.; Bernard, J. Special Quasirandom Structures. *Phys. Rev. Lett.* **1990**, *65* (3), 353–356.

(62) Cockayne, E.; van de Walle, A. Building Effective Models from Scarce but Accurate Data: Application to an Alloy Cluster Expansion Model. *Phys. Rev. B* **2010**, *81*, 12104–12113.

(63) van de Walle, A. Multicomponent Multisublattice Alloys, Nonconfigurational Entropy and Other Additions to the Alloy Theoretic Automated Toolkit. *Calphad* **2009**, *33*, 266–290.

(64) van de Walle, A. Methods for First-Principles Alloy Thermodynamics. *JOM - J. Min. Met. Mat. S.* **2013**, *65*, 1523–1532.

(65) Sawamura, M.; Kobayakawa, S.; Kikkawa, J.; Sharma, N.; Goonetilleke, D.; Rawal, A.; Shimada, N.; Yamamoto, K.; Yamamoto, R.; Zhou, Y.; et al. Nanostructured LiMnO2 with Li3PO4 Integrated at the Atomic Scale for High-Energy Electrode Materials with Reversible Anionic Redox. *ACS Cent. Sci.* **2020**, *6* (12), 2326–2338.

(66) Liu, H.; Zhu, Z.; Yan, Q.; Yu, S.; He, X.; Chen, Y.; Zhang, R.; Ma, L.; Liu, T.; Li, M.; et al. A Disordered Rock Salt Anode for Fast-Charging Lithium-Ion Batteries. *Nature* **2020**, *585* (7823), 63–67.

(67) Sathiya, M.; Rousse, G.; Ramesha, K.; Laisa, C. P.; Vezin, H.; Sougrati, M. T.; Doublet,

M.-L.; Foix, D.; Gonbeau, D.; Walker, W.; et al. Reversible Anionic Redox Chemistry in High-Capacity Layered-Oxide Electrodes. *Nat. Mater.* **2013**, *12* (9), 827–835.

(68) Glazier, S. L.; Li, J.; Zhou, J.; Bond, T.; Dahn, J. R. Characterization of Disordered Li(1+x)Ti2xFe(1-3x)O2 as Positive Electrode Materials in Li-Ion Batteries Using Percolation Theory. *Chem. Mater.* **2015**, *27* (22), 7751–7756.

(69) Wang, R.; Li, X.; Liu, L.; Lee, J.; Seo, D.-H.; Bo, S.-H.; Urban, A.; Ceder, G. A Disordered Rock-Salt Li-Excess Cathode Material with High Capacity and Substantial Oxygen Redox Activity: Li1.25Nb0.25Mn0.5O2. *Electrochem. commun.* **2015**, *60*, 70–73.

(70) Yabuuchi, N.; Takeuchi, M.; Nakayama, M.; Shiiba, H.; Ogawa, M.; Nakayama, K.; Ohta, T.; Endo, D.; Ozaki, T.; Inamasu, T.; et al. High-Capacity Electrode Materials for Rechargeable Lithium Batteries: Li3NbO4-Based System with Cation-Disordered Rocksalt Structure. *Proc. Natl. Acad. Sci. U. S. A.* **2015**, *112* (25), 7650–7655.

(71) Wang, C.; Ping, W.; Bai, Q.; Cui, H.; Hensleigh, R.; Wang, R.; Brozena, A. H.; Xu, Z.; Dai, J.; Pei, Y.; et al. A General Method to Synthesize and Sinter Bulk Ceramics in Seconds. *Science (80-.).* **2020**, *368* (6490), 521–526.

(72) Seymour, I. D.; Middlemiss, D. S.; Halat, D. M.; Trease, N. M.; Pell, A. J.; Grey, C. P. Characterizing Oxygen Local Environments in Paramagnetic Battery Materials via 17O NMR and DFT Calculations. *J. Am. Chem. Soc.* **2016**, *138* (30), 9405–9408.

(73) Zhang, K.; Jiang, Z.; Ning, F.; Li, B.; Shang, H.; Song, J.; Zuo, Y.; Yang, T.; Feng, G.; Ai, X.; et al. Metal-Ligand π Interactions in Lithium-Rich Li2RhO3 Cathode Material Activate Bimodal Anionic Redox. *Adv. Energy Mater.* **2021**, *11* (30), 2100892.

(74) Sathiya, M.; Abakumov, A. M.; Foix, D.; Rousse, G.; Ramesha, K.; Saubanère, M.; Doublet, M. L.; Vezin, H.; Laisa, C. P.; Prakash, A. S.; et al. Origin of Voltage Decay in

High-Capacity Layered Oxide Electrodes. *Nat. Mater.* **2015**, *14* (2), 230–238.

(75) James, A. C. W. P.; Goodenough, J. B. Structure and Bonding in Li2MoO3 and Li2−xMoO3 (0 ≤ x ≤ 1.7). *J. Solid State Chem.* **1988**, *76* (1), 87–96.

Acknowledgements

Funding: Z.Y. and C.W. (DFT calculations, analysis of results, and leadership of project) were supported as part of the Center for Electrochemical Energy Science (CEES), an Energy Frontier Research Center funded by the U.S. Department of Energy, Office of the Science, Basic Energy Science under award number DE-AC02-06CH11357. We gratefully acknowledge the computing resources from: 1) the National Energy Research Scientific Computing Center, a DOE Office of Science User Facility supported by the Office of Science of the U.S. Department of Energy under Contract DE-AC02-05CH11231, and 2) Blues, a high-performance computing cluster operated by the Laboratory Computing Resource Center at Argonne National Laboratory. Work performed at the Center for Nanoscale Materials, a U.S. Department of Energy Office of Science User Facility, was supported by the U.S. DOE, Office of Basic Energy Sciences, under Contract No. DE-AC02-06CH11357. **Author contributions:** The overall project was conceived by Z.Y., who also performed the DFT calculation of the ground-state structures, structural pathways, voltages, and energy densities. C.W. provided overall direction and advice for the project and analyzed the results. **Competing interests:** All authors declare that they have no competing interests. **Data and materials availability:** All data needed to evaluate the conclusions in the paper are present in the paper and/or the Supplementary Materials. Additional data related to this paper may be requested from the authors.

Figures

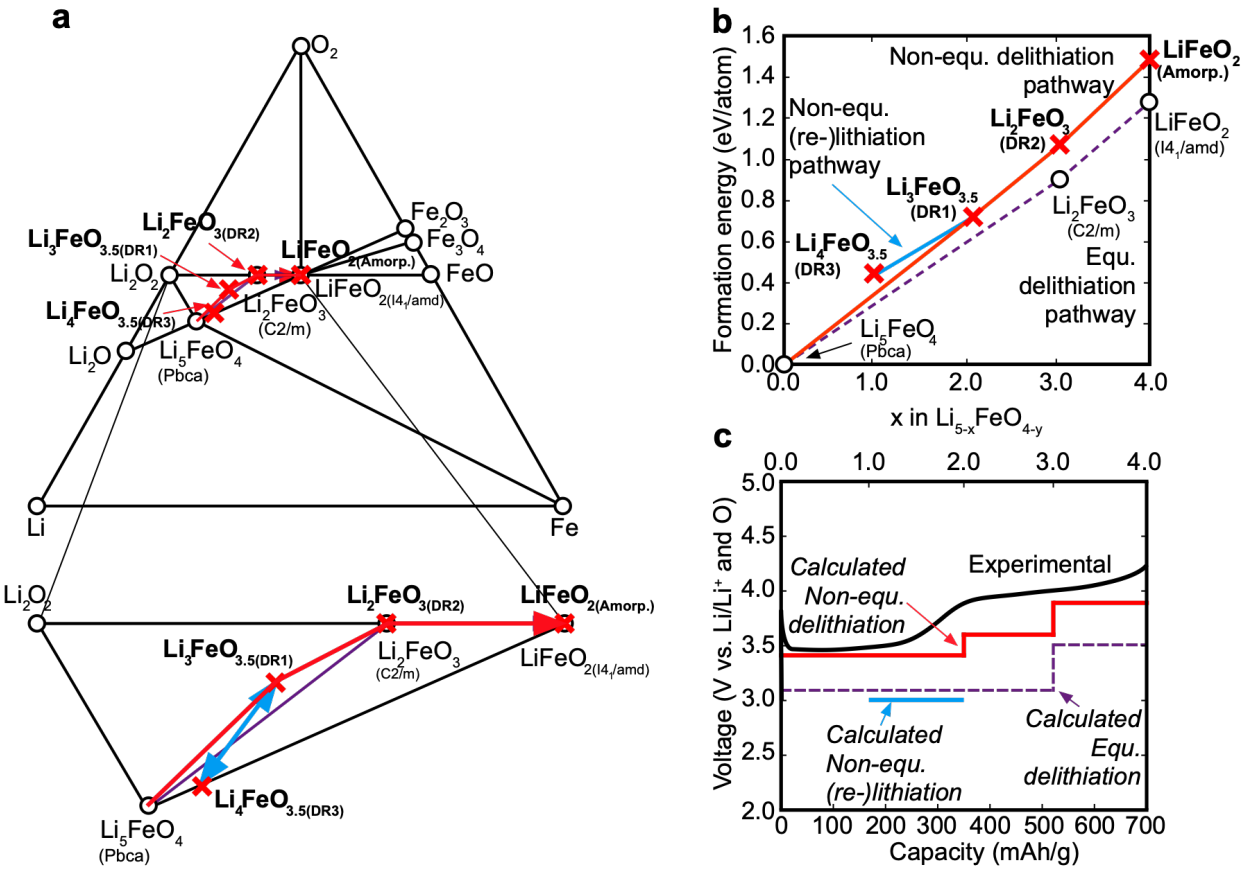

Figure 1. | Electrochemical delithiation and (re-lithiation) of Li_5FeO_4. (a) Calculated Li–Fe–O (T = 0 K) phase diagram and non-equilibrium/equilibrium delithiation pathways (red/purple) and the reversible (re-)lithiation reaction (blue). (b) Li_5FeO_4–$LiFeO_2$ convex hulls corresponding to the equilibrium/non-equilibrium delithiation pathways and reversible (re-)lithiation reaction with energetics from intermediate structures, the prototype structure, and known compounds. (c) Corresponding voltage profiles during the delithiation and (re-)lithiation of Li_5FeO_4; the non-equilibrium profile shows great agreement with the experimentally obtained charging curve.[12]

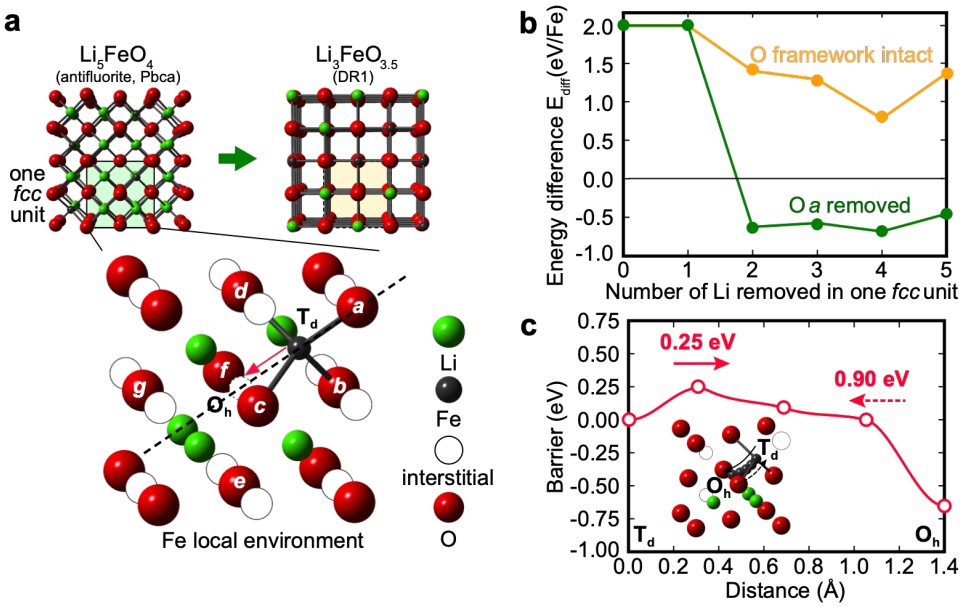

Figure 2. | Irreversible Fe migration during the antifluorite → disordered rocksalt phase transformation along with the delithiation. (a) Local environment of Fe in antifluorite Li_5FeO_4 and Fe migration path during the phase transition from antifluorite to disordered rocksalt structure. (b) Enabling of Fe migration by O removal. (c) Anisotropic energetic barrier during Fe migration.

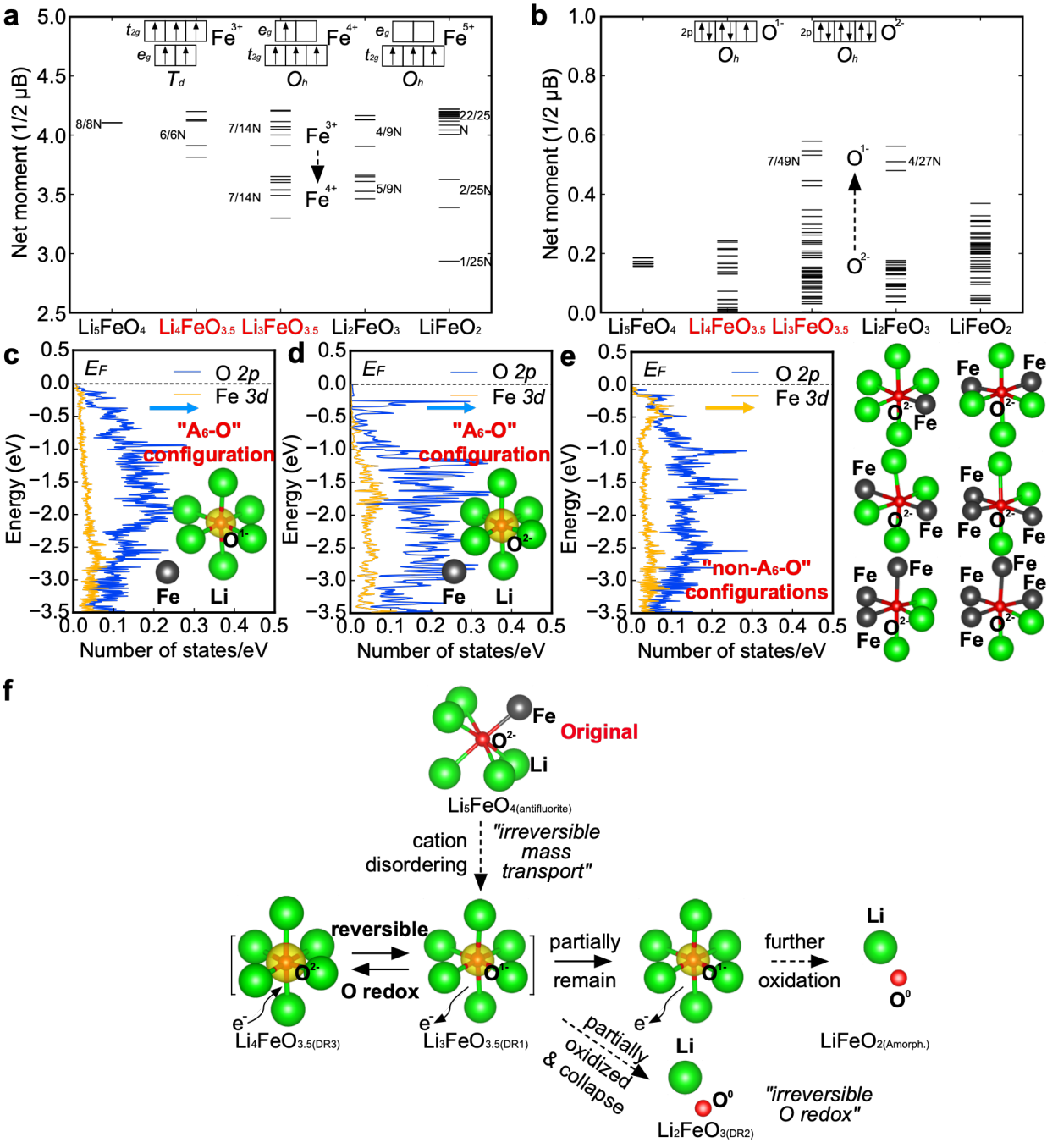

Figure 3. | Competing cationic (Fe) and anionic (O) redox activity during delithiation of Li_5FeO_4 and re-lithiation of $Li_3FeO_{3.5}$ to $Li_4FeO_{3.5}$. The evolution of the magnetization and oxidation state of (a) Fe and (b) O ions in intermediate phases $Li_{5-x}FeO_{4-y}$ (x = 0, 1, 2, 3, 4, y = 0, 0.5) during delithiation. *P*-DOS of O *2p* and Fe *3d* of (c) O^{1-} and (d) O^{2-} ions located in the Li_6–O local Li-excess configurations and the nearest Fe ions. Insets: isosurfaces of the charge density (yellow) around the O^{2-} and O^{1-} ions in the energy range of 0 to −1.0 eV. (e) O^{2-} ions located in the non-A_6–O configurations and the nearest Fe ions. (f)

Schematic illustration of "A_6–O" local Li excess configurations enabling the combined cationic and anionic redox in super alkali-rich Li_5FeO_4-based electrode materials.

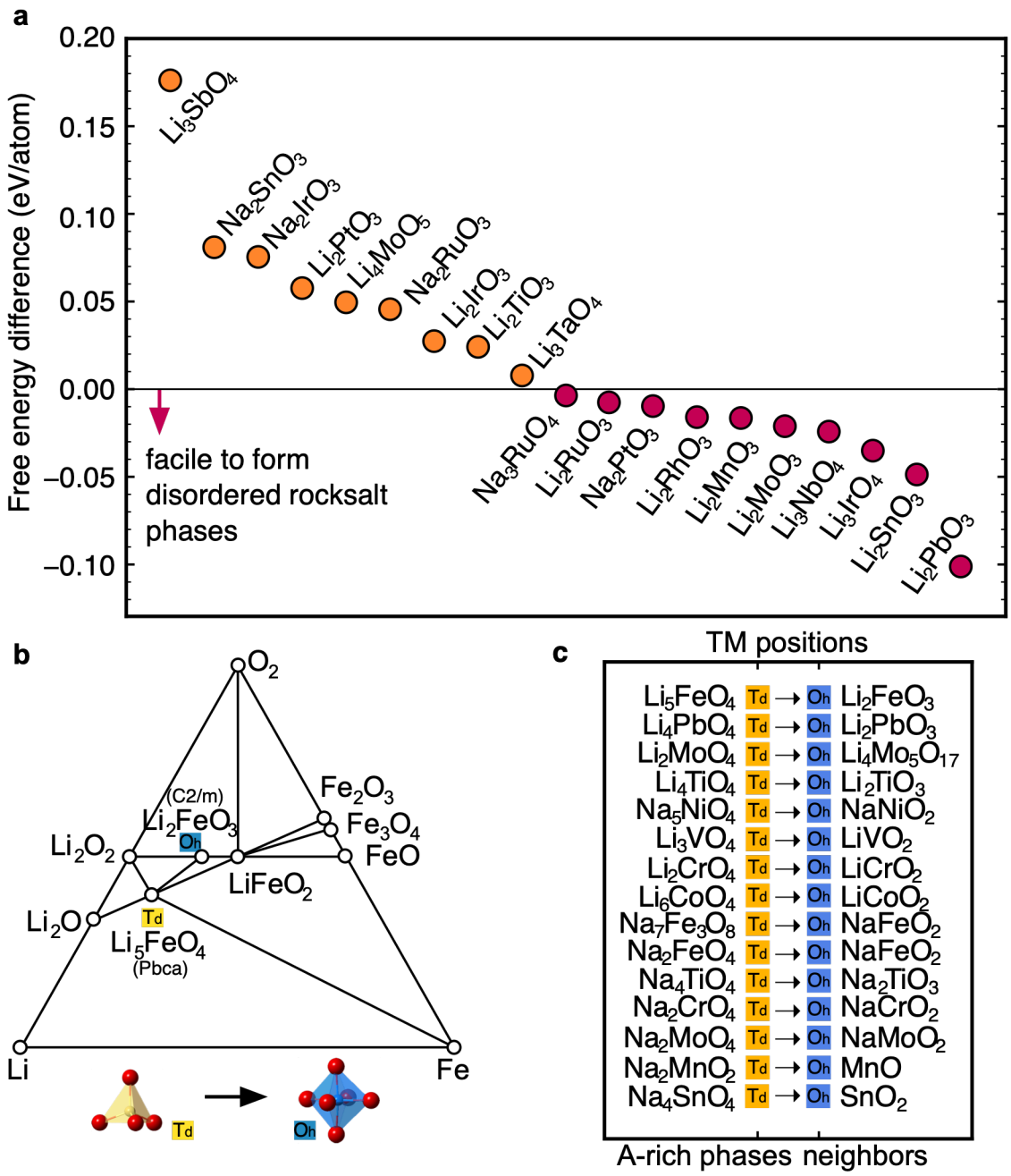

Figure 4. | High-throughput screening for super A-rich oxide based anionic-redox electrodes. (a) Identified candidates for potential DR phase synthesis, which exhibit the promise for unlocking the anionic redox activity. (b) Li-Fe-O phase diagram. Pristine Li_5FeO_4 with Fe located in the tetrahedral position and its closest neighbor of Li_2FeO_3 with Fe located in the octahedral position (c). Identified candidates which are possible to experience an electrochemical activation upon charge and ultimately enable the anionic redox activity.

Table 1. | Energetic impacts of different O on the Fe migration from the O_h to T_d site and Fe–O distance change upon Fe migration.

O removed	***a****	*b*	*c*	*d*	*e*	*f*	*g*
Fe–O distance change (Å)	+1.889	+0.378	−0.441	+0.369	−1.433	−1.497	−1.436
E_{diff}' (eV/Fe)	6.49	8.21	7.89	8.19	10.51	10.91	10.60

Table 2. | Transition metal positions in known super A-rich oxides and their closest neighbors in corresponding phase diagrams.

Super Li-rich oxide	TM position	Closest neighbor	TM position
Li_5FeO_4 (Pbca)	T_d	Li_2FeO_3 (C2/m)	O_h
Li_4PbO_4 (Cmcm)	T_d	Li_2PbO_3 (C2/c)	O_h
Li_2MoO_4 (R-3)	T_d	$Li_4Mo_5O_{17}$ (P-1)	O_h
Li_4TiO_4 (Cmcm)	T_d	Li_2TiO_3 (C2/c)	O_h
Li_3VO_4 (Pmn2_1)	T_d	$LiVO_2$ (R-3m)	O_h
Li_2CrO_4 (R-3)	T_d	$LiCrO_2$ (R-3m)	O_h
Li_6CoO_4 (P4_2/nmc)	T_d	$LiCoO_2$ (R-3m)	O_h
Li_2FeO_3 (C2/m)	O_h	$LiFeO_2$ (R-3m)	O_h
Li_4MoO_5 (P-1)	T_d	Li_2MoO_4 (R-3)	T_d
Li_2TiO_3 (C2/c)	O_h	$LiTiO_2$ (I4_1/amd)	O_h
$Li_6Zr_2O_7$ (C2/c)	O_h	Li_2ZrO_3 (Cc)	O_h
Li_2ZrO_3 (Cc)	O_h	ZrO_2 (P2_1/c)	PB
Li_8IrO_6 (R-3)	O_h	Li_3IrO_4 (C2/m)	O_h
Li_3IrO_4 (C2/m)	O_h	Li_2IrO_3 (C2/m)	O_h
Li_2IrO_3 (C2/m)	O_h	IrO_2 (P4_2/mnm)	O_h
Li_8PtO_6 (R-3)	O_h	Li_2PtO_3 (C2/m)	O_h
Li_2PtO_3 (C2/m)	O_h	PtO_2 (Pnnm)	O_h
Li_8SnO_6 (R-3)	O_h	Li_2SnO_3 (C2/c)	O_h
Li_2SnO_3 (C2/c)	O_h	SnO_2 (P4_2/mnm)	O_h
Li_7SnO_6 (R3)	O_h	Li_5SnO_5 (C2/m)	O_h
Li_5SnO_5 (C2/m)	O_h	Li_3SnO_4 (P2/c)	O_h
Li_3SnO_4 (P2/c)	O_h	$LiSnO_4$ (Pnna)	O_h
$Li_8Sn_2O_9$ (P-1)	O_h	Li_3NbO_4 (I23)	O_h
Li_3NbO_4 (I23)	O_h	$LiNbO_3$ (R3c)	O_h
Li_7TaO_6 (P3)	O_h	Li_3TaO_4 (C2/c)	O_h
Li_3TaO_4 (C2/c)	O_h	$LiTaO_3$ (R3c)	O_h
Li_2MnO_3 (C2/c)	O_h	$LiMnO_2$ (I4_1/amd)	O_h
Li_2MnO_2 (P-3m1)	O_h	MnO (Fm-3m)	O_h
Li_2RuO_3 (C2/c)	O_h	$LiRuO_2$ (Pnnm)	O_h
Li_8CoO_6 (P6_3cm)	T_d	Li_6CoO_4 (P4_2/nmc)	T_d
Li_2RhO_3 (C2/m)	O_h	$LiRhO_2$ (R-3m)	O_h
Li_2NiO_3 (C2/m)	O_h	$LiNiO_2$ (C2/m)	O_h
Li_2NiO_2 (P-3m1)	O_h	NiO (Fm-3m)	O_h

Super Na-rich oxide	TM position	Closest neighbor	TM position
$Na_7Fe_3O_8$ (Pbca)	T_d	$NaFeO_2$ (R-3m)	O_h
Na_2FeO_4 (Cmcm)	T_d	$NaFeO_2$ (R-3m)	O_h
Na_5NiO_4 (Pbca)	T_d	$NaNiO_2$ (C2/m)	O_h
Na_4SnO_4 (P-1)	T_d	SnO_2 (P4_2/mnm)	O_h
Na_4TiO_4 (P-1)	T_d	Na_2TiO_3 (C2/c)	O_h
Na_2CrO_4 (Cmcm)	T_d	$NaCrO_2$ (R-3m)	O_h
Na_2MoO_4 (Fd-3m)	T_d	$NaMoO_2$ (R-3m)	O_h
Na_2MnO_2 (Fddd)	T_d	MnO (Fd-3m)	O_h
Na_5FeO_4 (Pbca)	T_d	Na_3FeO_3 (P2_1/c)	T_d
Na_4FeO_4 (P-1)	T_d	Na_3FeO_3 (P2_1/c)	T_d
Na_3FeO_3 (P2_1/c)	T_d	$Na_7Fe_3O_8$ (P-1)	T_d
Na_2TiO_3 (C2/c)	O_h	$NaTiO_2$ (R-3m)	O_h
Na_6ZnO_4 (P6_3mc)	T_d	Na_2ZnO_2 (P2_1/c)	T_d
Na_2ZnO_2 (P2_1/c)	T_d	$Na_2Zn_2O_3$ (P2_1/c)	T_d
Na_5NbO_5 (C2/c)	TB	$NaNbO_2$ (P6_3/mmc)	TA
Na_5TaO_5 (C2/c)	TB	$NaTaO_3$ (Cmcm)	O_h
Na_4CrO_4 (P-1)	T_d	Na_2CrO_4 (Cmcm)	T_d
Na_4MoO_5 (P-1)	SP	Na_2MoO_4 (Fd-3m)	T_d
$Na_{14}Fe_2O_9$ (P-3)	T_d	Na_5MnO_4 (Pmn2_1)	T_d
Na_5MnO_4 (Pmn2_1)	T_d	$Na_4Mn_2O_5$ (Fddd)	SP
$Na_4Mn_2O_5$ (Fddd)	SP	$NaMnO_2$ (C2/m)	O_h
Na_3RuO_4 (C2/m)	O_h	Na_2RuO_3 (C2/c)	O_h
Na_2RuO_3 (C2/c)	O_h	$NaRuO_2$ (R-3m)	O_h
Na_2RuO_4 (P2_1/c)	TA	$Na_2Ru_2O_5$ (P4/mmm)	TA
Na_4IrO_4 (P2_1/c)	SA	$NaIrO_3$ (R-3m)	O_h
Na_2PtO_3 (Fddd)	O_h	$NaPt_3O_4$ (Pm-3n)	SA
Na_6PbO_5 (I4mm)	SP	Na_4PbO_4 (P-1)	T_d
Na_4PbO_4 (P-1)	T_d	Na_2PbO_2 (Pbcn)	other
Na_2PdO_3 (C2/c)	O_h	$Na_2Pd_3O_4$ (Immm)	SA

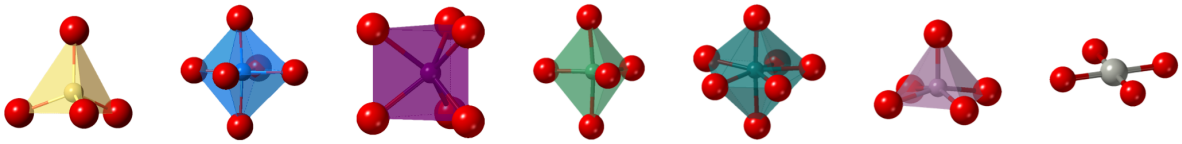

Tetrahedral (T_d) | Octahedral (O_h) | Trigonal Antiprismatic (TA) | Trigonal Bipyramidal (TB) | Pentagonal Bipyramidal (PB) | Square Pyramidal (SP) | Square Planar (SA)